



High bandwidth optical coherent transient true-time delay
by Randy Ray Reibel

A dissertation submitted in partial fulfillment of the requirements for the degree of Doctor of
Philosophy in Physics
Montana State University
© Copyright by Randy Ray Reibel (2002)

Abstract:

An approach to reaching high bandwidth optical coherent transient (OCT) true-time delay (TTD) is described and demonstrated in this thesis. Utilizing the stimulated photon echo process in rare-earth ion doped crystals, such as Tm³⁺:YAG, TTD of optical signals with bandwidths > 20 GHz and high time bandwidth products > 10⁴ are possible. TTD regenerators using OCT's have been demonstrated at low band-widths (< 40 MHz) showing picosecond delay resolutions with microsecond delays. With the advent of high bandwidth chirped lasers and high bandwidth electro-optic phase modulators, OCT TTD of broadband optical signals is now possible in the multi-gigahertz regime.

To achieve this goal, several theoretical and technical aspects had to be explored. Theoretical discussions and numerical simulations are given using the Maxwell-Bloch equations with arbitrary phase. These simulations show good signal fidelity and high (60%) power efficiencies on echoes produced from gratings programmed with linear frequency chirps. New approaches for programming spectral gratings were also examined that utilized high bandwidth electro-optic modulators. In this technique, the phase modulation sidebands on an optical carrier are linearly chirped, creating an analog to the common linear frequency chirp. This approach allows multi-gigahertz true-time delay spectral grating programming. These new programming approaches are examined and characterized, both through simulation and experiment.

A high bandwidth injection locked amplifier, based on semiconductor diode lasers, had to be developed and characterized to boost optical powers from both electro-optic phase modulators as well as chirped lasers. The injection locking system in conjunction with acousto-optic modulators were used in high bandwidth TTD demonstrations in Tm³⁺:YAG. Ultimately, high bandwidth binary phase shift keyed probe pulses were used in a demonstration of broadband true-time delay at a data rate of 1 GBit/s. The techniques, theory, and demonstrations described in this thesis can also be applied to high bandwidth optical signal processing and arbitrary waveform generation using optical coherent transient phenomena.

HIGH BANDWIDTH OPTICAL COHERENT
TRANSIENT TRUE-TIME DELAY

by

Randy Ray Reibel

A dissertation submitted in partial fulfillment
of the requirements for the degree

of

Doctor of Philosophy

in

Physics

MONTANA STATE UNIVERSITY
Bozeman, Montana

May 2002

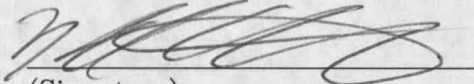
D378
R2709

APPROVAL

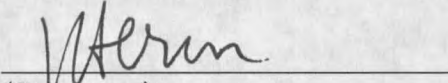
of a dissertation submitted by

Randy Ray Reibel

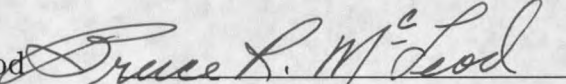
This dissertation has been read by each member of the dissertation committee and has been found to be satisfactory regarding content, English usage, format, citations, bibliographic style, and consistency, and is ready for submission to the College of Graduate Studies.

Wm. Randall Babbitt  5/13/02
(Signature) Date

Approved for the Department of Physics

John C. Hermanson  5-13-02
(Signature) Date

Approved for the College of Graduate Studies

Bruce R. McLeod  5-21-02
(Signature) Date

STATEMENT OF PERMISSION TO USE

In presenting this dissertation in partial fulfillment of the requirements for a doctoral degree at Montana State University, I agree that the Library shall make it available to borrowers under rules of the Library. I further agree that copying of this dissertation is allowable only for scholarly purposes, consistent with "fair use" as prescribed in the U. S. Copyright Law. Requests for extensive copying or reproduction of this dissertation should be referred to Bell & Howell Information and Learning, 300 North Zeeb Road, Ann Arbor, Michigan 48106, to whom I have granted "the exclusive right to reproduce and distribute my dissertation in and from microform along with the non-exclusive right to reproduce and distribute my abstract in any format in whole or in part."

Signature



Date

5/13/02

ACKNOWLEDGEMENTS

This dissertation could not have happened without the help of so many people. First, let me thank my advisor, Dr. W. Randy Babbitt, for allowing me the opportunity to be a part of this challenging research project. Dr. Babbitt's fundamental grasp on OCT's and his ability to teach others are the main reasons this dissertation even exists. Randy, thank you for your years of kindness, support, and smiles.

I want to thank Dr. Mingzhen Tian, the Research Scientist in our group. Without her encouragement, instruction and leadership this thesis would not exist. Mingzhen, thanks for listening to me, answering my questions, and staying awake during those late hours in the lab.

I want to thank all my fellow group members. I need to give special thanks to Zeb Barber for his outstanding help and also his wonderful friendship. To Zhiqiang Jia, without whose help the injection locking simulator would not exist. Thanks to Spectrum Lab employees Zachary Cole and Kris Merkel for their constant help, frisbee golf, and unique perspectives on life. I want to also thank Pete Roos, for his friendship, answers, and memories climbing.

Finally, love and thanks to all of my family. To my wife Sandra Lynn, for your incredible, unbelievable support, strength and sacrifice through these years. Your love inspires and captures me. To Ransom for insisting I play once in a while. And to Maggie for her wagging tail and midnight walks.

TABLE OF CONTENTS

LIST OF TABLES	viii
LIST OF FIGURES	ix
1. INTRODUCTION TO HIGH BANDWIDTH OPTICAL COHERENT TRANSIENTS.....	1
Introduction To Research Topic.....	1
Overview of Thesis	10
2. THEORETICAL OVERVIEW OF OPTICAL COHERENT TRANSIENTS	14
Optical Coherent Transients And The Photon Echo	15
Properties Of OCT Media	15
Spectral Hole Burning	17
Spectral Gratings and The Photon Echo.....	19
Possible Methods of Solution For The Photon Echo	27
Exact Solutions	33
Fourier Transform Approximation	34
Bloch Equations Of Motion.....	35
Thin Crystal $\alpha L \ll 1$	35
Thick Crystal $\alpha L \gtrsim 1$, Weak Pulses $\Theta \ll 1$	36
Thick Crystal $\alpha L \gtrsim 1$, Area Theorem Approach.....	37
Maxwell-Bloch With Arbitrary Phase	39
Two Level Systems and the Bloch Equations.....	41
Maxwell-Bloch Derivation	47
Maxwell-Bloch Simulations	54
3. PRACTICAL CONSIDERATIONS FOR HIGH BANDWIDTH OCT PROGRAMMING	65
Material Considerations	66
OCT Programming Efficiencies and Considerations	68
Grating Efficiency vs. Bandwidth	70
Highly Efficient TTD Using Chirped Programming.....	75
Accumulation of Spectral Gratings	83
Spatial Gratings and Spatially Isolated Echoes.....	86
Coherent and Incoherent Saturation Effects	88
Optical Modulation and Detection Considerations	93
Phase Modulation And Spectral Filtering	94
Spectral Filtering and Efficient Detection.....	98

4. BROADBAND INJECTION LOCKING AS AN AMPLIFIER	106
Semiconductor Diode Lasers And Injection Locking Theory.....	108
Experiments	117
Initial Injection Locking and Locking Regions.....	121
CW Phase Modulation	128
Broadband Operation (BPSK).....	133
5. TEMPORALLY OVERLAPPED LINEAR FREQUENCY CHIRPED PULSES	138
Chirped Pulse Programming	139
Phase Matching Conditions	145
Low Bandwidth Demonstrations	147
Experimental Setup.....	147
Delay Versus Frequency Offset.....	148
Operating Conditions.....	155
Low Bandwidth Accumulation Experiments	159
Demonstrations Showing the Dynamics of Accumulation.....	160
Simulations Showing the Dynamics of Accumulation	163
High Bandwidth Experiments	172
6. LINEAR SIDEBAND CHIRPS AND THEIR APPLICATION	182
Linear Sideband Chirps.....	183
Spatial-Spectral Grating Programming.....	190
Phase Matching	195
Initial Demonstrations	198
High Bandwidth Single Laser Experiments	201
High Bandwidth Double Laser Experiments	210
Delay vs Frequency Offset and T_2	214
CW Amplitude Modulation	217
TTD of Broadband Data.....	228
7. SUMMARY.....	237
Maxwell-Bloch Theory and Simulations	239
Injection Locking.....	241
Temporally Overlapped LFC's	242
Linear Sideband Chirp Programming.....	243
Future Research Directions.....	243
APPENDICES	247
APPENDIX A – DYNAMICS OF BROADBAND ACCUMULATED GRATINGS	248
APPENDIX B – NUTATION OF STIMULATED PHOTON ECHOES.....	255

APPENDIX C – ARBITRARY WAVEFORM GENERATION USING LINEAR SIDEBAND CHIRPS	279
REFERENCES CITED.....	296

LIST OF TABLES

Table	Page
1. Expected and measured inverse chirp rates for echoes from figure 43 along with RMS deviations	149

LIST OF FIGURES

Figure	Page
1. The operational design of how a phased array system works	3
2. (a) Shows a typical Gaussian shaped inhomogeneously broadened transition made up of individual Lorentzian lines from atoms at different frequencies. (b) The transition after being illuminated by a laser with frequency f_L . The lower trace shows a hole in the transition, where the electrons have been transferred to the excited state, upper trace	18
3. Experimental demonstration of the two pulse photon echo (2PE) and the stimulated photon echo (SPE). In this figure, the temporal pulse widths were $\tau_p = 100$ ns and $\tau_{21} = 1100$ ns. Experiment performed by the author	20
4. (a) Shows the two programming pulses, FWHM ≈ 1 ns, $\tau_{21} = 10$ ns. (b) Shows the resulting power spectrum. (c) The expected output as calculated using non-causal linear filter theory. One can see the SPE and the non-causal virtual echo, or VE	24
5. Quadratic fits predicted from linear filter theory (solid and labeled with "Q") and numerical solutions (dashed and labeled with "MB") for the 2PE and the SPE power efficiencies. Here the quadratic solution was valid only for $\alpha L \ll 1$. The numerical solutions were found using a full Maxwell-Bloch treatment of the medium and give a more realistic picture of the true behavior of the system. Here $\Theta_1 = \Theta_2 = \Theta_3 = \pi/2$	29
6. A diagram showing different approaches to a predictive tool for photon echoes. Each pulse in a sequence should be treated with this "roadmap". One asks the specific questions about the pulse, slowly traveling through the "roadmap", marking down the specific conditions, and equations along the way. Once an output is reached an equation for the polarization, P , should have been determined as well as an equation for the output field in terms of that P . Solution types can be mixed, see text for discussion	31

7. A screen shot of the Maxwell-Bloch simulator's graphical user interface used to enter parameters and start simulations 55
8. A simulated echo sequence showing the 2PE and the SPE for an $\alpha L = 1.4$ 56
9. The population grating, stored in the r_3 component of the Bloch vector versus detuning at time $5 \mu s$ from the above echo sequence. The top plot shows the grating for an $\alpha L \approx .3$, and the bottom plot shows the grating for an $\alpha L \approx .3$ 57
10. The field amplitude for various times and absorption length of the first two pulses and the 2PE 58
11. The field amplitude for various times and absorption length of the probe pulse and the SPE 59
12. The simulated power efficiencies for 2PE (o's) and SPE (x's) are shown versus absorption length. The solid line is the quadratic analytic solution with a coefficient of $1/4$. Here $\tau_1 \gg \tau_2 = \tau_3$, and the pulse areas were $\Theta_1 = 0.01\pi$, $\Theta_2 = 0.5\pi$, and $\Theta_3 = 0.5\pi$ 61
13. The input and output intensities for a chirped pulse sequence from a crystal with $\alpha L = 1.4$. Here the echo efficiency is $\sim 20\%$ 64
14. The r_3 component of the Bloch vector as a function of the detuning. This shows the spectral grating created by two linear frequency chirped pulses. Here $\alpha L = 1.4$ and $t = 5 \mu s$ 64
15. The atomic levels of interest for this thesis for the rare-earth ion doped crystal $Tm^{3+}:YAG$ 68
16. Data points showing simulated peak echo height versus bandwidth for constant programming powers. Here $\tau_C = 4 \mu s$ and δ is varied to keep τ_D constant. The solid line is calculated using the analytic functional dependence of $1/B^2$ (normalized). The dashed line is a plot of the analytic dependence of a brief pulse programming versus bandwidth and is normalized to the first point in the $1/B^2$ sequence for contrast. The triangles are simulated sequences for a constant τ_C/B ratio with efficiencies given by the right hand axis 73

17. Illustrations of each of the simulated input sequences studied for this thesis. In (a) a data storage configuration is shown. This configuration has shown better than unit efficiencies (see text) and is simulated here for comparison with new arbitrary phase Maxwell-Bloch simulator. (b) A brief programming pulse scheme for programming TTD echo sequences. (c) A linear frequency chirped programming scheme for producing TTD echo sequences 76
18. Power efficiencies for the data storage programming scheme shown in figure 17 (a). Here $\Theta_1 = \Theta_P = A$ and range from 0.1 to 0.7 π . The first and third pulses were Guassian pulses with FWHM's of 0.1 ns. Here, the data pulse was also Guassian and had a FWHM of 0.4 ns and $\Theta_2 = 0.01\pi$ 78
19. Power efficiencies for the brief pulse TTD programming scheme shown in figure 17 (b). Here $\Theta_1 = \Theta_2 = A$ and range from 0.1 to 0.9 π . The first and second pulses were Guassian with FWHM's of 0.1 ns. The data pulse was also Guassian and had a FWHM of 0.2 ns and $\Theta_P = 0.05 \pi$ 79
20. Power efficiencies for the linear frequency chirped pulse TTD programming scheme shown in figure 17 (c). Here $\Omega_1 = \Omega_2 = \Omega$ and ranges from 5 GRad/s to 19 GRad/s. The programming bandwidth was $B = 50$ GHz and $\tau_C = 1$ ns. The data pulse was Guassian and had a FWHM of 0.04 ns and $\Theta_P = 0.05 \pi$ 80
21. A simulation of bi-phase, amplitude modulated data undergoing highly efficient TTD. The input is the dotted line. The solid line is the output at $\alpha L = 3.06$ where the efficiency is close to 60%. This is more approximately twice the efficiency from the brief pulse programming scheme. Here the bits had FWHM's = 0.04 ns and $\Theta_{bit} = 0.02\pi$. The programming chirps had $\pi/2$ equivalent $\Omega = 12$ GRad/s, $B=50$ GHz, and $\tau_C = 1$ ns 83
22. The typical propagation directions for an SPE experiment in the box-car configuration. Here 1, 2, and 3 represent the directions of pulses 1, 2 and 3, and e represents the direction for which the echo would propagate after the crystal 87
23. An optical pulse that has experienced Rabi oscillations 89

24. Echoes from various strength quasi-continuous optical probe pulses. The echo shows the nutational effects that are described with theory and experiment in appendix 2	92
25. The power spectrum of a simulated CW phase modulated signal on a carrier.....	96
26. The reflection function of a fabry-perot etalon that is 3 mm thick measured using a frequency scan of a diode laser	100
27. The strength of the intensity modulation at the modulation frequency for various detunings and modulation frequencies for experimental phase modulated signals.....	102
28. Simulated strengths of the intensity modulation at the modulation frequency for various detunings and modulation frequencies using linear filter theory. Frequency axes units are in the FWHM of the filter	103
29. The operational premise for a laser injection locking system	109
30. The simulated optical spectra for an injection locked slave laser with a free running frequency of 200 GHz showing the standard period doubling route to chaos with $\Omega_o = 0$, and (a) $\xi = 0.0013$, (b) $\xi = 0.0027$, (c) $\xi = 0.0077$, (d) $\xi = 0.0183$	117
31. Optical injection locking setup using a fiber coupled integrated optics phase modulator. See text for discussion	119
32. Optical spectra of (a) master laser, (b) slave laser before injection locking, and (c) slave laser after injection locking	122
33. Optical spectrum of the different regions on the period doubling route to chaos showing (a) Stable locking, (b) undamped relaxation oscillations, (c) period doubled relaxation oscillations, and (d) the chaotic region	124

34. Observed regions of injection locking versus the detuning, Δ and the injection ratio, ζ for a $P_{out} = 88$ mW. The symbols represent observations of the boundaries between different regions while the lines and shading are there to guide the eye. The various regions are stable locking (S), undamped relaxation oscillations (P1), period doubled relaxation oscillations (P2), chaotic regions (C), four wave mixing (4W), multi-longitudinal mixing (M), period four relaxation oscillations (P4), an undefined region of both chaos and relaxation oscillations (U), as well as unlocked regions 127
35. (Left) CW phase modulation of the master laser with modulation frequencies of (a) 1 GHz, and (b) 3 GHz. (Right) Plot of the peak powers vs. modulation frequency for the carrier and sidebands of the phase modulated master. At each modulation frequency the rf power was adjusted to achieve roughly a 2:1 ratio of carrier to sidebands 129
36. Injection locked peak powers vs. modulation frequency for (a) lower frequency first order sideband, (b) carrier, and (c) upper frequency first order sideband. The different power levels correspond to gains of $A = 14, 18, 20, 22$ and 23 dB 130
37. The residual amplitude modulation for both the phase modulated master and the injection locked signal. A deviation at around 3 GHz is apparent 133
38. Bits 1 through 15 of the delayed-self-heterodyne injection locked outputs of BPSK data at (a) 2 Gbit/s, (b) 3 Gbit/s, and (c) 6 Gbit/s. The expected output is shown as dotted lines. To the right of the data sequence is the eye diagram for the total 256 bit test sequence 137
39. Input sequences and expected echo for (a) Two LFC's separated by a delay τ_{21} (b) Two temporally overlapped LFC's. Solid lines represent amplitude and dashed lines represent frequency 140
40. Diagram of a typical temporally overlapped linear frequency chirped pulse experiment 146
41. Echoes from a probe pulse shown for various frequency offsets from $\delta = 3$ MHz to 19.8 MHz in steps of 1.2 MHz. Here $B = 40$ MHz and $\tau_C = 3 \mu\text{s}$ 150

42. Simulated programming and probe pulses and the echo output for various frequency offsets, $\delta = 0.66$ MHz to 19.785 MHz in steps of 2.125 MHz. Here $\tau_C = 3 \mu s$ and $B = 40$ MHz 150
43. Measured echo delays vs. frequency offset for several different τ_C 's with linear fits using (5.1). The points for $\tau_C = 30$ and $100 \mu s$ demonstrate the reduced chirp rate requirements..... 151
44. (Top) Data points and a best fit line for the time delay versus frequency offset of the $3 \mu s$ data shown in the previous figure. Here the method to measure the time delay was a Gaussian fit to the echo peaks. (Bottom) The residuals of the above data points giving an RMS = 1.6 ns 152
45. An example of a true time delayed data sequence (right x30). Here $\tau_c = 100 \mu s$ with a programmed time delay of 625 ns. The data sequence (left) is 101011001 at a data rate of 20 Mbit/s 154
46. The simulated r_3 component of the Bloch vector versus detuning for a single LFC pulse. Notice that the chirp undergoes chirping oscillations. Here $B = 40$ GHz, $\tau_C = 1$ ns, and $\alpha L = 0.3$ 155
47. The simulated r_3 component of the Bloch vector versus detuning for several different temporally separate LFC pulses. Notice both the rapid oscillations (the spectral grating with period $1/\tau_D$ and the chirp envelope. Here $B = 40$ GHz, $\tau_C = 1$ ns and $\alpha L = 0.3$ 156
48. The simulated r_3 component of the Bloch vector versus detuning for temporally overlapped LFC pulses. The two plots show two different frequency offsets, and show that the spectral envelopes of the spectral grating changes leading to the possibility of intensity fluctuations in the echo. Here $B = 40$ GHz, $\tau_C = 5 \mu s$ and $\alpha L = 0.3$ 157
49. Experimental echo intensities plotted versus delay time for (a) TBP = 40, (b) TBP = 120, and (c) TBP = 200. For TBP < 120, a periodic intensity fluctuation is observed 158
50. Echo power efficiencies vs. programming number (lower axis) or time (upper axis) for a frequency stabilized Ti:Sapphire laser system locked to a spectral hole. The different plots are various programming strengths (Rabi frequency, Ω) as shown in the legend. Here $\tau_c = 1 \mu s$, $B = 40$ MHz, $\tau_D = 250$ ns, and $\tau_r = 31 \mu s$ 164

51. Echo intensities vs. programming number (lower axis) or time (upper axis) using the injection locked ECDL laser system. The different plots are various programming strengths (Rabi frequency, Ω) as shown in the legend. Here $\tau_c = 1\mu s$, $\tau_d = 125ns$, and $\tau_r = 46\mu s$ 165
52. Simulated accumulation sequences with $\tau_C = 1\mu s$, $\tau_D = 250\text{ ns}$, and $\tau_r = 31\mu s$. The echo power efficiencies are plotted versus programming number (lower axis) or time (upper axis). The different lines represent different programming strengths (Rabi frequency, Ω) with (a) showing programming Rabi frequencies from $\Omega = 0.3\text{ MRad/s}$ to 1.2 MRad/s in steps of 0.1 MRad/s , and (b) showing programming Rabi frequencies from $\Omega = 1.3\text{ MRad/s}$ to 1.8 MRad/s in steps of 0.1 MRad/s , then to 2.8 MRad/s in steps of 0.2 MRad/s 166
53. Grating accumulation sequences for $\Omega = 0.5\text{ MRad/s}$ with $\tau_C = 1\mu s$, $\tau_D = 250\text{ ns}$, and $\tau_r = 31\mu s$. The r_3 components are plotted versus detuning and programming number 169
54. Grating accumulation sequences for $\Omega = 1.2\text{ MRad/s}$ with $\tau_C = 1\mu s$, $\tau_D = 250\text{ ns}$, and $\tau_r = 31\mu s$. The r_3 components are plotted versus detuning and programming number 169
55. Grating accumulation sequences for $\Omega = 2.8\text{ MRad/s}$ with $\tau_C = 1\mu s$, $\tau_D = 250\text{ ns}$, and $\tau_r = 31\mu s$. The r_3 components are plotted versus detuning and programming number 170
56. Overall gratings versus detuning at $N = 900$ for (a) $\Omega = 0.5\text{ MRad/s}$ programming, (b) $\Omega = 1.2\text{ MRad/s}$ programming, and (c) $\Omega = 2.8\text{ MRad/s}$ programming pulses 172
57. Diagram of the high bandwidth CECDL experiment utilizing temporally overlapped linear frequency chirped pulses..... 174
58. A low intensity LFC optical probe pulse before (dashed line) and after (solid line) transmission through the medium with an $\alpha L = 1.4$. Here $\tau_c = 15\text{ ns}$ and $B = 15\text{ GHz}$, giving a chirp rate, $\gamma = 1\text{ GHz/ns}$ 176
59. (a) This figure shows the transmission of a low intensity 2.4 GHz LFC probing a 2.0 GHz TTD grating programmed with the TOLFC method. The large oscillation on the transmission is a frequency oscillation corresponding to a grating period $1/\tau_D$ where $\tau_D = 0.22\mu s$.
(b) Shows these oscillations in greater detail 177

60. This figure shows echo intensity of a 50 ns probe pulse versus the optical frequency of the probe pulse (data points). The solid line shows the expected position of the programmed TTD grating 178
61. This figure examines the experimental echo peak heights as a function of grating bandwidth created with the CECDL laser system. Here the programming power and τ_C are kept constant, $\tau_C = 4 \mu\text{s}$ and the offset frequency is kept at $\delta = 20 \text{ MHz}$. The solid line is a fit using a functional dependence of $1/B^2$ according to eqn. (3.6) 181
62. This figure examines the experimental echo delay times versus the optical frequency of the 50 ns probe pulse. The echo delay time can be seen to decrease indicating non-linearities in the LFC pulse 181
63. An example of r_3 of a linear sideband chirped pulse after passing through the medium. Here the bandwidth of the LSC is 20 GHz and the start frequency is 25 GHz. Note the start of the second order chirps at approximately 60 GHz 185
64. A plot of the functional dependence of $J_1(\beta)^2/J_2(\beta)^2$ (right hand axis) as well as the square of $J_1(\beta)$ and $J_2(\beta)$. The maximum of $J_1(\beta)^2/J_2(\beta)^2$ occurs at 0 and an acceptable level must be chosen 186
65. (a) A chirping sine wave used as a drive voltage. (b) A digital approximation to the chirping sine wave 188
66. (top) The power spectrum of a square wave phase chirp on a carrier. (bottom) The power spectrum of a regular phase chirp on a carrier. In each case the chirps have $\tau_C = 1 \mu\text{s}$, $B = 0.2 \text{ GHz}$, $\beta = \pi/2$, and a 10 GHz carrier 189
67. The effect of two temporally overlapped frequency offset linear sideband chirped pulses incident upon the medium. Here the r_3 component of the Bloch vector is plotted as a function of frequency 192
68. Programming and probe pulses created by separate laser sources. Here the programming pulses are LSC pulses and the probe pulse frequency f_{L2} is centered on the up-shifted first order grating 193

69. An input pulse diagram for a single laser experiment. This experiment utilizes the same laser to create the programming and probe pulses. Here the probe pulses have a CW phase modulation that pushes first order sidebands to the center frequency of the grating allowing echoes to be produced 195
70. A simulation showing the output of three separately detuned probe pulses. The detunings are -32 MHz, 0 MHz and +32 MHz for the first, second and third pulse respectively..... 199
71. An experimental demonstration of LSC programming, showing the output of three separately detuned probe pulses. The detunings are -12 MHz, 0 MHz and +12 MHz for the first, second and third pulse respectively 201
72. The experimental setup for the single laser, collinear programming and probing method 203
73. Example echoes from the single laser LSC programming technique. Here the echoes are shown for various frequency offsets with a 20 MHz bandwidth detection limit. See text for discussion 205
74. Echo outputs observed on the fast detector showing the beat frequency of the spatially overlapped echoes at $2f_m = 2.85$ GHz for various δ 's ... 206
75. An overview of how to use the single laser method to create data pulses discussed in the text 208
76. A 500 MBit/s amplitude modulated echo sequence (lower) created by modulating β in eqn. (6.1) as described in the text. The expected bit sequence is shown as the upper trace..... 210
77. The experimental setup for the high bandwidth two laser experiments . 212
78. Various echoes produced from a temporally brief (50 ns) probe pulse. Here various δ 's were chosen to give several different τ_D 's..... 215
79. Experimentally determined delay times versus frequency offset (triangles) for the echoes in 78. The solid line is a linear fit to the data giving an RMS deviation of 0.45 ns. This RMS deviation was found from the residuals plotted in the lower portion of the figure 217

80. (a) Shows a spectral grating programmed with two LFC's. (b) Shows a phase modulated probe signal situated such that only the carrier and higher frequency sidebands will be diffracted from the grating in (a), producing an amplitude modulated echo at the programmed delay. 219
81. A plot of several output echoes from a CW phase modulated probe with $f_m = 0.5$ GHz for various frequency offsets 220
82. The relative delay of the first peak in the amplitude modulated echoes from figure 81 as a function of frequency offset (circles). The solid line is a linear fit to the data. The expected slope is $71.42 \mu\text{s}/\text{MHz}$. The residuals are plotted in the lower figure from which an RMS deviation of 52 ps was found 222
83. An example of the power spectrum of the amplitude modulated data in figure 81 (circles). The theoretical shape of this power spectrum is also plotted (solid line) 224
84. The phase of the Fourier transformed data from figure 81 plotted against the relative delay (circles). A linear fit to the data is shown (solid line). The expected slope is 3.14 rad/ns . The residuals are also shown and give an RMS deviation of 0.14 radians 225
85. A plot of several output echoes from a CW phase modulated probe with $f_m = 1.0$ GHz for various frequency offsets 226
86. The phase of the Fourier transformed data from figure 85 plotted against the relative delay (circles). A linear fit to the data is shown (solid line). The expected slope is 6.28 rad/ns . The RMS deviation was calculated to be 0.38 radians from the residuals plotted in the lower portion 227
87. A 1 GBit/s BPSK modulated probe pulse (lower) is shown with the heterodyned echo signal (upper). The echo signal has the expected 80 ns delay 230
88. Zoom of the delayed 1 GBit/s BPSK echo signal from figure 87 is compared to the expected echo signal. There are no bit errors in the echo sequence 232
89. A sequence of heterodyned BPSK echoes with $\Gamma_D = 666 \text{ MBits/s}$ is shown for various δ 's 233

- 90. A $10 \mu\text{s}$ long heterodyned BPSK echo with $\Gamma_D = 666 \text{ Mbits/s}$. Here the detector's lower bandwidth is 10 MHz producing the high pass filtered appearance..... 234
- 91. Several different 200 ns sections of the echo output in figure 90. No bit errors are observable for the echo output 236
- 92. (a) Three echo pulses created from a single probe pulse. (b) Arbitrary heights produced on the three echoes 281

ABSTRACT

An approach to reaching high bandwidth optical coherent transient (OCT) true-time delay (TTD) is described and demonstrated in this thesis. Utilizing the stimulated photon echo process in rare-earth ion doped crystals, such as $\text{Tm}^{3+}:\text{YAG}$, TTD of optical signals with bandwidths > 20 GHz and high time bandwidth products $> 10^4$ are possible. TTD regenerators using OCT's have been demonstrated at low bandwidths (< 40 MHz) showing picosecond delay resolutions with microsecond delays. With the advent of high bandwidth chirped lasers and high bandwidth electro-optic phase modulators, OCT TTD of broadband optical signals is now possible in the multi-gigahertz regime.

To achieve this goal, several theoretical and technical aspects had to be explored. Theoretical discussions and numerical simulations are given using the Maxwell-Bloch equations with arbitrary phase. These simulations show good signal fidelity and high (60%) power efficiencies on echoes produced from gratings programmed with linear frequency chirps. New approaches for programming spectral gratings were also examined that utilized high bandwidth electro-optic modulators. In this technique, the phase modulation sidebands on an optical carrier are linearly chirped, creating an analog to the common linear frequency chirp. This approach allows multi-gigahertz true-time delay spectral grating programming. These new programming approaches are examined and characterized, both through simulation and experiment.

A high bandwidth injection locked amplifier, based on semiconductor diode lasers, had to be developed and characterized to boost optical powers from both electro-optic phase modulators as well as chirped lasers. The injection locking system in conjunction with acousto-optic modulators were used in high bandwidth TTD demonstrations in $\text{Tm}^{3+}:\text{YAG}$. Ultimately, high bandwidth binary phase shift keyed probe pulses were used in a demonstration of broadband true-time delay at a data rate of 1 GBit/s. The techniques, theory, and demonstrations described in this thesis can also be applied to high bandwidth optical signal processing and arbitrary waveform generation using optical coherent transient phenomena.

CHAPTER 1

INTRODUCTION TO HIGH BANDWIDTH OPTICAL
COHERENT TRANSIENTS

The goal of this thesis is to describe and demonstrate an approach to reaching high bandwidth optical coherent transient (OCT) true-time delay. True-time delay (TTD) is useful in a number of potential applications including phased array antenna systems, arbitrary waveform generation and correlators. This chapter presents an introduction to this research topic including a brief overview of stimulated photon echoes (SPE). The potential usefulness of photon echoes in these high bandwidth systems is examined and an overview of how to reach these bandwidths is shown. An overall description and the organization of this thesis is also given.

Introduction To Research Topic

In Merriam-Webster's Online Collegiate Dictionary the word echo has the definition: *the repetition of a sound caused by reflection of sound waves* [1]. Most all of us are familiar with the effect of an acoustic or reflection echo. Whether we were in a large auditorium, outside near a building or inside some room, an echo is the repetition of our words caused by a reflection of the sound waves from some surface. Echoes are unique in that they mimic or repeat the words of the person who uttered them although often the echo is fainter or a less intense sound. The amount of time

it takes before an echo reaches an observer is directly proportional to the distance the observer is from the surface that has reflected the sound. Thus by changing the distance to the reflecting surface an echo's time delay can be varied. In much the same way, a photon echo, generated from an OCT process, follows these traits, however, the waveform is no longer an acoustic wave but an electromagnetic wave. The photon echo is not created by reflection from a surface, it is instead created by a complex physical process in an optically absorbing material. In certain situations the photon echo waveform will exactly mimic the original electromagnetic waveform, however with less intensity and a variable time delay. These characteristics are similar to the acoustic echo and are what gives rise to the name *photon echo*. But the photon echo is much more than a simple reflection from a surface and the OCT processes that govern it are truly unique and can be used as a powerful optical processing tool for a variety of applications.

One such application for the photon echo is as a component that can control, steer and adaptively beamform phased array antennas. Phased array antennas, steered with conventional electronics, currently perform a variety of tasks and find application to both military and civilian markets. These systems make use of the wavelike properties of electromagnetic radiation to "steer" beams without ever physically moving the antenna. The significant benefits of such systems over conventional radar systems were quickly noticed and several phased array radar systems became operational in the 1960's [2]. The operational premise of such a system is shown in figure 1. These

arrays can be used to transmit or receive a variety of waveforms. The array antenna is a collection of RF emitters, each emitting its individual electromagnetic field. In the far field, the electromagnetic fields of each emitter sum to form the overall beam pattern from the antenna array.

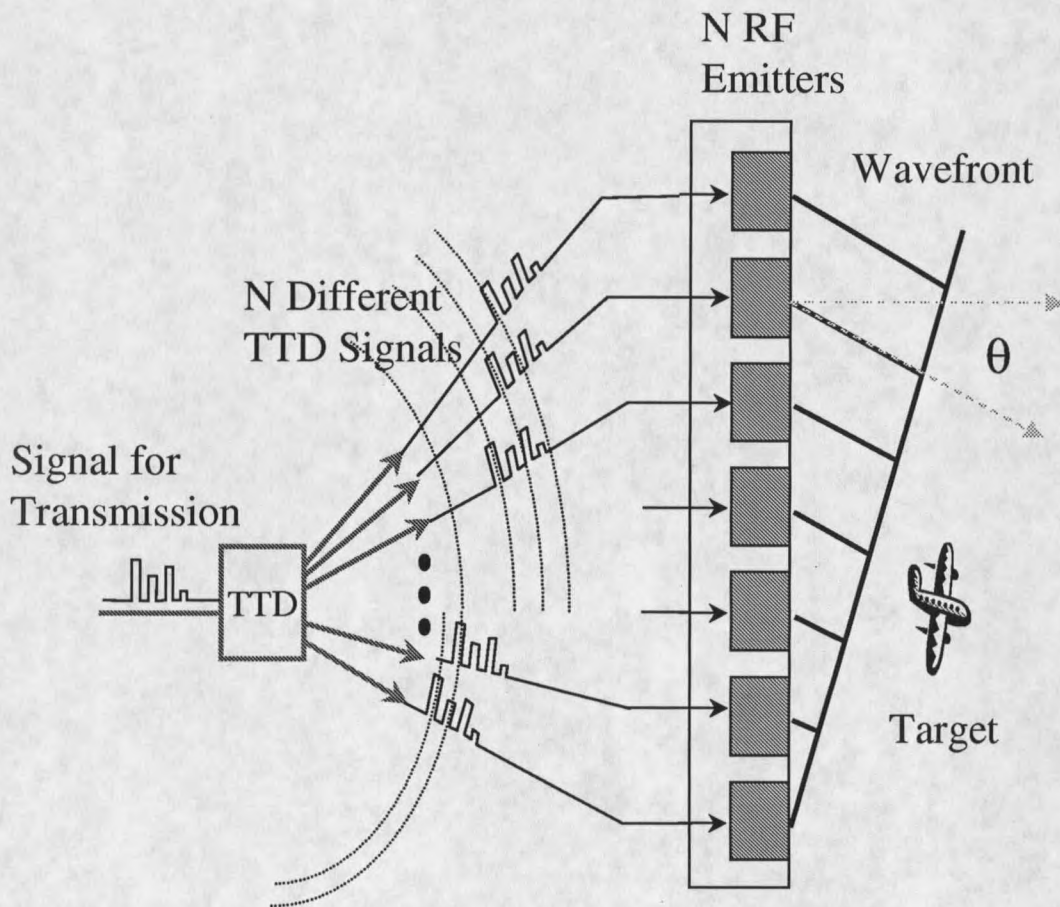


Figure 1. The operational design of how a phased array system works.

This overall beam pattern in the far field is known as the antenna beam lobe. This lobe can be controlled or steered utilizing the wave-nature of electromagnetic fields. If the time delay from each emitter to a spatial location away from the array can be controlled, the signal at that spatial location can be made to constructively or destructively interfere with the field produced at that location from other emitters. In the far field, the delay imparted to the electromagnetic fields from each emitter allows the beam lobe to be steered as shown in figure 1. Thus, the time delay of the electrical signals becomes the key component to the operation of a phased array radar. In narrow band (nearly single frequency) antenna arrays, the time delay of an electrical signal need not be *true* time delay. Instead, the electrical signal can be simply phase shifted. A single frequency sinusoidal waveform that is phase shifted is equivalent to one that is time delayed. Thus, simple electronic phase shifting devices could be used to steer the antenna, assuming the waveform is close to a single frequency sinusoidal waveform (narrow band) or, in other words, has a low fractional bandwidth (bandwidth divided by carrier). As the bandwidth deviates from narrowband an equal phase shift no longer translates directly to an equal time delay of the whole waveform. Essentially, different frequency components getting the same phase shift from the phase shifter, have a time delay, τ_D , that can be written as

$$\tau_D(\omega_m) = \phi/\omega_m. \quad (1.1)$$

Here ϕ is the constant phase shift imparted by the phase shifting device, and ω_m is

a frequency component of the broadband signal. If the fractional bandwidth of the signal is large, one can see that different ω_m 's will experience different time delays, τ_D . This causes signals with significant bandwidths to behave improperly when steered with phase shifting devices. This imparts what is known as beam squint on the main lobe of the radiation field emitted from the array elements. Since delay and angle are related in a phased array, beam squint essentially means the steering of different frequency components of the signal into different angular directions. This angular spread, $\Delta\theta$, is given by

$$\Delta\theta = -\frac{B}{\omega_{RF}} \tan(\theta) \quad (1.2)$$

Here, B is the bandwidth of the signal, ω_{RF} is the carrier frequency of the radar (giving a fractional bandwidth B/ω_{RF}), and θ is the steering angle of the main lobe [3]. As can be seen, the angular deviation is a linear function of the fractional bandwidth, giving large angular deviations of frequency components for large fractional bandwidths. It should be noted that the angular size of the antenna beam lobe gets smaller with more antenna elements. Thus, if a large phased array radar (with high fractional bandwidths) uses phase shifters to control the time delay, beam squint will be a significant problem [4].

In order for a system of antenna elements to properly steer signals with large fractional bandwidths, the elements must impart a true-time delay (TTD) on the signals. TTD means that each frequency component of the signal for a given emitter gets the same time delay rather than the same phase shift. Thus, eqn. (1.1) can be

rearranged as

$$\phi(\omega_m) = \omega_m \tau_D. \quad (1.3)$$

In a TTD system it is τ_D that typically remains constant (per element), and thus the phase shift needed will change according to the given frequency component, ω_m . Producing broadband TTD waveforms is the main emphasis of this thesis.

There have been many proposals for optical TTD control of an RF signal. These include but are not limited to delaying optical signals via different optical delay lines or creating delays by frequency shifting the optical carrier in a highly dispersive optical fiber [3]. In the first approach, several different techniques have been envisioned but all follow the same principle. That principle is that one would choose the time delay for the optical signal by switching the optical pulse into an appropriate delay line. One suggestion is to use several different length optical fibers to give various different delays. Unfortunately, as the number of array elements grows, the switching network for such a system becomes increasingly complex as does the amount of fiber needed. For the second approach, simply by changing the frequency of the optical carrier a different delay can be chosen because the index of refraction for that frequency has changed. In this case, it is the number of distinctive frequency channels that can be achieved by the optical source that limits the resolution of the delays to less than 1 part in 1000 [3]. Along with this, a tunable diode laser and fiber must be used for each element of the array. Again, this results in an increasing complexity and cost as the number of array elements is increased. These systems also have no ability to

control the phase, number, or weight of these delays, and thus adaptive beamforming or jammer nulling can not be done with such systems.

It has been suggested that the SPE process can be used to create the TTD needed to avoid beam squint in a phased array radar or communication system [5]. Instead of using an electronic phase shifter, the photon echo would be used to create TTD. The properties of OCT's are such that the photon echo can theoretically delay signals with tens of gigahertz bandwidths over delays of microseconds with picosecond resolutions. The delays can be programmed on the fly or preprogrammed. The storage capabilities of OCT's enable several different delays to be stored spatially in the OCT medium providing more than a million different delays all within a single compact crystal. This along with the ability to individually control the delay of each frequency component makes OCT's an attractive basis for steering a phased array antenna, especially ones requiring adaptive beamforming and jammer nulling.

In order to create a stimulated photon echo, an inhomogeneously broadened absorber (IBA), such as a rare-earth ion doped crystal, is used. Because of the special properties of IBA's, a time delay between two incident brief programming pulses is stored as a spectral grating within the medium. This grating can be probed sometime later by another incident brief pulse. The medium is then coherently stimulated and produces a stimulated photon echo with the delay that was stored in the spectral grating. In the linear regime, this process is not limited to just temporally brief probe pulses. Any arbitrarily shaped incident probe pulse can be delayed assuming

the bandwidth of the spectral grating is larger than the bandwidth of the probe.

OCT's have previously been demonstrated as TTD devices giving microsecond delay times and picosecond resolutions [6]. Various methods including brief pulse programming and chirped pulse programming have been explored to produce TTD spectral gratings [7]. However, almost all previous demonstrations were over a limited bandwidth (typically 40 MHz) and did not reach the ideal goal of showing TTD with multi-gigahertz bandwidths. This thesis extends TTD demonstrations to the gigahertz bandwidth, along with developing more practical OCT techniques to program multi-gigahertz TTD.

Programming and probing broadband spectral gratings is not an easy task. In order to program an efficient spectral grating, a significant amount of optical energy must be transferred to the medium. Unfortunately, if brief pulses are used to program these broadband gratings, their temporal lengths must be extremely short (on the order of 100 picoseconds) to achieve large bandwidths. Producing these types of brief pulses is not easy, requiring the use of mode-locked lasers with amplification. These systems are impractical because of their cost, power inefficiencies and size. And, even though powerful pulsed lasers exist with tremendous power per pulse (\sim GW), producing efficient broadband spectral gratings with these lasers has proven challenging. The intensities required are near or exceed the damage threshold of OCT crystals. Processes such as accumulation of spectral gratings, where less powerful programming pulses are repeatedly applied to the medium, must be used in order to produce

efficient gratings.

Another way to produce a spectral grating in an OCT media is through the use of linear frequency chirped pulses [7]. Linear frequency chirps (LFC's) ramp their instantaneous frequency linearly as a function of time. Through the proper choice of chirp bandwidth and chirp duration, a power limited laser can program much more efficient TTD spectral gratings, as compared to brief pulses from the same laser. High bandwidth (> 20 GHz) LFC's are now a possibility due to the recent advances in chirped external cavity diode lasers (CECDL's) [8, 9].

Broadband signals are also inherently harder to detect because of noise issues. The level of thermal noise detected increases as the square root of the bandwidth. Thus, this thermal noise limits the detection of broadband echoes. Poor echo efficiencies also contribute to these detection problems. Recently, photon echoes with greater than unit efficiency have been suggested and observed for certain situations using optically thick samples [10, 11]. Unfortunately, the direct results from these research efforts are not applicable to TTD. This thesis examines the efficiencies of photon echoes for the situation of TTD for both brief pulse programming and LFC programming in optically thick crystals. Another problem is that these broadband RF signals must be imparted to the optical carrier, TTD, and subsequently converted to RF signals. The TTD optical signals must be detected in a fashion that allows detection of the encoded broadband signals. Various methods of modulation and detection are explored. It is also shown that the spectral grating itself can be utilized in making more efficient

detection methods for optically encoded broadband signals.

Another reason previous demonstrations were limited to low bandwidths (40 MHz) was the lack of suitable high bandwidth modulators to create probe signals. Advancements in high bandwidth, affordable electro-optic modulators (EOM's) makes the encoding of high bandwidth electronic signals onto optical carriers easier. Unfortunately, at the wavelength with which most of our work is done (793 nm) these EOM's are optical power limited due to photorefractive damage. The maximum output powers are 1 to 2 orders of magnitude lower than that required to produce detectable broadband photon echoes. In order to overcome this power limitation, a suitable amplifier for high bandwidth signals was developed using EOM's and an injection locked amplifier.

Overview of Thesis

This thesis details the possible approaches for creating high bandwidth TTD along with the problems and solutions. As stated above TTD applications such as phased array radars and communication systems will benefit from this research. But, as with any type of science, there are other unexpected benefits from the research and other applications to which this research can be applied. The desire to bring OCT's into the high bandwidth regime is a continuing struggle, one that is ongoing with new developments and twists everyday. This thesis is a snapshot of the past three years detailing the steps and barriers that had to be overcome before high bandwidth TTD

could be realized. What follows is a brief description of the chapters found within this thesis.

In chapter 2, the theoretical framework needed for this thesis is developed and presented. This includes a detailed overview of the stimulated photon echo process and the linear filter theory that predicts the dynamics of this process in certain regimes. An outline of other approaches to predictive solutions is given for various conditions. Chapter 2 also includes a discussion on the Maxwell-Bloch equations including arbitrary phases of the field. This mathematical approach, combined with simulation, allows quantitative predictions of the OCT phenomena covered in this thesis. Specifically, high efficiency TTD is studied for thick crystals utilizing linear frequency and linear phase chirps. Aspects such as delay resolution and signal fidelity are also examined with this simulator.

Chapter 3 presents the important practical considerations for reaching high bandwidth TTD using the stimulated photon echo process. A discussion of phase modulated signals created from high bandwidth EOM's is given. Spectral filtering effects caused by the medium as well as programmed spectral gratings are examined for these high bandwidth signals. It is shown that detection schemes utilizing these spectral filters can be more efficient than conventional detection schemes. Experimental parameters and material details are discussed as well as problems related to temporally long probe pulses. Simulations are performed for optically thick samples, showing that expected echo efficiencies using chirped programming can reach 60%.

The chapter also examines the aspects of accumulation and continuous programming and continuous processing, which are relevant to this thesis.

Chapter 4 shows how to amplify broadband signals from the power limited EOM's using an injection locking system. The needed theoretical framework for injection locking is detailed as well as experimental demonstrations of the amplifier. The benefits of such a system include ease of use and gains of more than 20 dB. However, using injection locking with semiconductor diode lasers has inherent challenges that will be discussed.

Through experimental demonstrations, problems related to high bandwidth linear frequency chirped programming were uncovered that called for modifying the previous approach to linear frequency chirp programming. Chapter 5 presents the modification of the linear frequency chirped programming method. The modification was to temporally overlap two frequency offset linear frequency chirps. Both low bandwidth demonstrations and high bandwidth demonstrations (using a CECDL) are presented. The tuning linearity of this method is examined as well as the efficiency of programmed gratings for TTD versus bandwidth scaling. Results from accumulation using this new method are also presented.

Finally, a novel technique for programming TTD gratings into an OCT medium using the broadband EOM's is presented in chapter 6. By using an EOM in conjunction with the injection locked amplifier, one can create multi-gigahertz gratings in the OCT media. This novel technique relies upon linear sideband chirping (LSC) and in

chapter 6 this approach is detailed. Experimental TTD results of both data and CW waveforms, which are delayed over several hundreds of nanoseconds, are presented. Data rates of 1 Gbit/s and bandwidths of 1 GHz are achieved. The tuning linearity and the resolution of this method are also analyzed.

CHAPTER 2

THEORETICAL OVERVIEW OF OPTICAL COHERENT
TRANSIENTS

A basic overview of OCT's followed by the development of the coupled Maxwell-Bloch equations is given in this chapter. The basic operation of OCT's in the linear regime (energetically weak pulses) can be understood from a simple conceptual framework using a Fourier transform approach. In optically thin media, one can invoke the undepleted pump approximation that assumes the output electric field is proportional to the polarization of the thin medium. Using this approximation, the output electric field is a linear transform of the input pulses. While this is useful in describing the output from the medium, the assumptions invoked mean working in a regime of poor power efficiencies. By including the effects of propagation, where the polarization acts back on the field, highly efficient photon echoes can be created in optically thick media [10, 12, 13, 11]. To do this, the Maxwell wave equation must be used in conjunction with the optical Bloch equations that describe the dynamics of the medium. Expressions that can be solved analytically for certain cases have been shown [13] for the coupled Maxwell-Bloch equations (assuming energetically weak pulses or temporally brief pulses). The analytic solutions found were compared with direct numerical integrations of the Maxwell-Bloch equations and were found to be in good agreement [13]. However, the previous approaches to solving the propagation

effects of the medium did not allow for arbitrary phase and frequency for the input pulses [10, 12, 13]. The phase can not be ignored for pulses that are linearly chirped such as those used in this thesis. Here, a derivation for the Maxwell-Bloch equations is given for arbitrary phase and frequency. These equations are then used as the basis for a Maxwell-Bloch simulator that can predict the output of pulses with arbitrary phase and frequency in an optically thick regime. This allows analysis of the echo power efficiency for linear frequency chirped programming pulses.

Optical Coherent Transients And The Photon Echo

Properties Of OCT Media

In order to begin a discussion on the photon echo, it helps to understand some of the basic properties of the medium in which photon echoes can take place. Photon echoes have been observed in various kinds of media ranging from inorganic rare-earth-ion-doped crystals, such as Tm^{3+} :YAG [14], to gases of heated materials, such as barium or sodium heated in an oven [15], and even to amorphous systems of large organic molecules [16]. All of these materials, as varied as their physical makeup is, contain similar physical properties, which allow them to produce the photon echo.

First, like any optical phenomena, there must be an optical transition between two atomic levels in the material of interest. This allows a given atom within the medium to become excited, by absorbing a photon. Once an atom is in an excited state, it can leave the excited state through either spontaneous emission or stimulated

emission. The spontaneous emission decay rate Γ_e , gives rise to an exponential decay of the upper state with lifetime, $T_1 = 1/2\pi\Gamma_e$. The upper state lifetime is important in the photon echo process, as it determines the lifetime of the upper state spectral grating.

For the photon echo process, there is a fundamental limit to the amount of time delay that can be created. This limit arises due to the coherence lifetime or irreversible dephasing time in the crystal. This lifetime is given as $T_2 = 1/\pi\Gamma_H$, where Γ_H is the homogeneous linewidth. In an inorganic crystal, this individual atomic linewidth is created due to perturbations such as lattice phonon coupling, nuclear and electron spin couplings as well as the overall population decay rate. It is known as the "homogeneous" linewidth because the broadening is experienced equally by all atoms within the medium. For demonstrations in $\text{Tm}^{3+}:\text{YAG}$, Γ_H is mostly dominated by phonon coupling and is thus heavily dependent upon temperature [17]. Typical homogeneous linewidths for rare-earth ion doped crystals used in this thesis are tens of kilohertz, but have been measured to be as narrow as 122 Hz [18].

Another broadening mechanism, called inhomogeneous broadening, exists within these crystals. Due to imperfections within a rare-earth ion doped crystal, the local environment of a given ion can be perturbed resulting in a different resonant frequency for the ion. Since the perturbations add randomly, the inhomogeneous line typically has a Gaussian lineshape. Because the inhomogeneous broadening plays such a critical role in OCT phenomena these materials are often referred to as inhomogeneously

